ACS APPLIED POLYMER MATERIALS

pubs.acs.org/acsapm

Forum Article

Cross-linking Poly(caprolactone)−Polyamidoamine Linear Dendritic Block Copolymers for Theranostic Nanomedicine

Indika Chandrasiri, Mahesh Loku Yaddehige, Bo Li, Yuzhe Sun, William E. Meador, Austin Dorris, Mohammad Farid Zia, Nathan I. Hammer, Alex Flynt, Jared H. Delcamp, Edward Davis, Alexander Lippert, and Davita L. Watkins*

Cite This: https://doi.org/10.1021/acsapm.1c01131

Read Online

ACCESS | Metrics & More | Article Recommendations | Supporting Information

ABSTRACT: This study represents a comparative analysis of the solution behavior and self-assembly pattern of two linear dendritic block copolymers (LDBCs) composed of a generation 3 polyamidoamine (PAMAM) dendron as the dendritic block and poly(caprolactone) (PCL) as the linear block, the latter of which is modified with pendant phenyl groups. Phenyl substituents were introduced to induce physical cross-linking in LDBC nanoparticles via $\pi-\pi$ stacking. A synthetic strategy was developed to access phenyl substituted LDBCs through an ε-caprolactone monomer derivative followed by ring-opening polymerization to form a library of LDBCs with yields above 83%. Polymersome-like nanoparticles were observed in water with a 74.4 nm average diameter. Cross-linked LDBC nanoparticles demonstrated a 37.1% relative decrease in the critical aggregation concentration (CAC) and a 27.3−41.2% relative increase of hydrophobic loading efficiency relative to unsubstituted LDBCs. Nanoparticles loaded with a potential photothermal agent (phenyl indolizine-C5 (C5)) showed a photothermal efficiency of 49.4% with a heating temperature of 44.4 °C. These nanoparticles were efficiently loaded into HEK293 cells with cell viability above 87.5% at the highest concentration. Upon illumination with red light, nanoparticles loaded with photothermal agent were able to induce cell death in cancer cells. This work suggests that the phenyl substituted LDBCs form nanoparticles with enhanced stability and loading efficiencies compared to conventional nonphenylated systems and display a greater potential to be used as nanocarriers in theranostic nanomedicine.

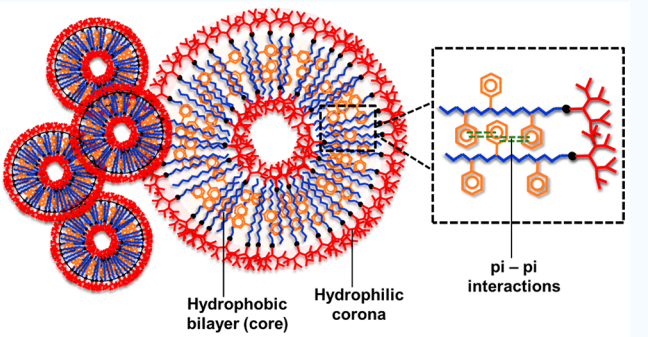

KEYWORDS: *nanomedicine, photothermal therapy, NIR imaging, theranostics, self-assembly, nanoparticles*

INTRODUCTION

Nanomedicine has become an emerging topic in the fields of therapeutic delivery, disease diagnosis, and medical imaging. Over recent decades, nanomedicine has shown remarkable success in clinical cancer therapy.[1−3] In contrast with conventional molecular-based therapeutics, nanoparticle-based strategies offer the advantage of combining target specific therapy and high resolution imaging into one system.[4] Additionally, such strategies have been shown to address the drawbacks of traditional medicine and chemotherapy, such as nonselective accumulation, poor retention, low solubility, and high toxicity toward healthy cells.[5,6]

Nanoplatforms such as liposomes, polymeric micelles, and polymersomes have been closely studied and established as promising modalities for diagnosis and treatment. Specifically, polymersomes made from biocompatible amphiphilic block copolymers have recently emerged as promising nanocarriers to replace liposomes and conventional micellular nanocarriers for targeted and controlled delivery of hydrophobic and hydrophilic therapeutics.[7−14] Although polymersomes are known for their stability compared to liposomes and polymeric micelles, conventional nanocarriers tend to disintegrate before reaching the target disease site due to systemic dilution, blood temperature, pH incompatibility, and ionic strength.[15−17] Moreover, interactions between the bloodstream components, specifically plasma proteins and the polymersomes' building blocks (unimers), lead to the premature release of the therapeutic agents and suboptimal therapeutic responses.[18−20]

Cross-linking is known to be simple and straightforward yet a reliable method to minimize premature disintegration, thereby assuring enhanced circulation times with sustained release of the therapeutic agents.[5,21] There are two main

Special Issue: Early Career Forum

Received: September 1, 2021
Accepted: December 21, 2021

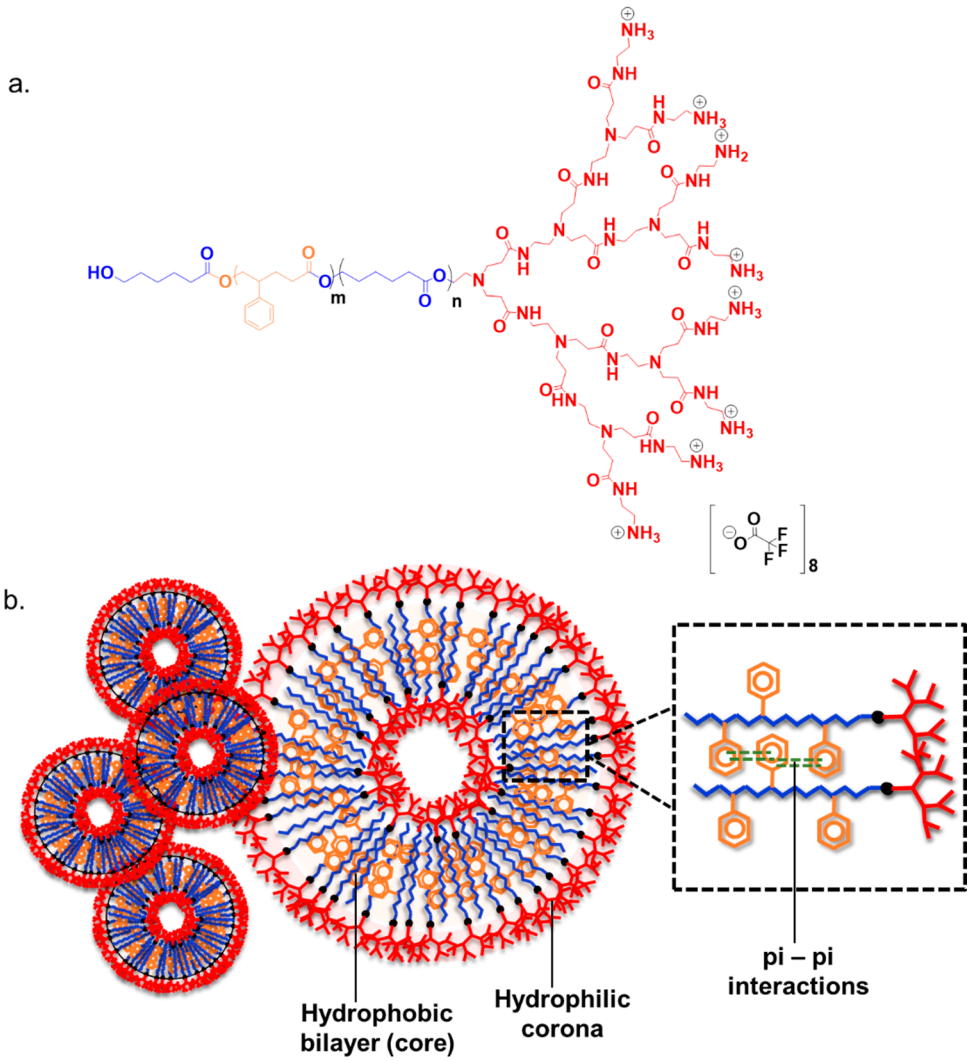

Figure 1. (a) General ChemDraw depiction of PhPCL-G3 LDBC. (b) Graphical representation of PhPCL-G3 LDBCs forming polymersome-like nanoparticles in water via physical cross-linking induced by $\pi-\pi$ interactions.

approaches to cross-linking with regard to the bonding type: covalent (chemical) cross-linking and noncovalent (physical) cross-linking. While the typical driving force for self-assembly is based on hydrophobic interactions, in cross-linked nanoparticles, there are additional attractive forces between unimers. The formation of the cross-links can be done in either the core or the corona of the nanoparticle. These added interactions improve the mechanical stability of the nanoparticles and keep them intact upon a higher degree of dilution. However, applications have been limited due to the excessive synthetic steps, inability to self-repair after being disintegrated or damaged (before reaching the target site), and weak responsiveness toward external stimuli.[22−24]

Noncovalent cross-linking is more dynamic and yields self-repairing properties without requiring excessive synthetic steps.[5,21,25,26] Therefore, it has drawn more attention in application perspectives. Noncovalent cross-linking can be categorized according to the cross-linking mechanism: hydrogen (H)-bonding, $\pi-\pi$ stacking, dipole−dipole interactions, hydrophobic interactions, and coordination complexing. These noncovalent interactions form multiple bonds among unimers and stabilize the nanoparticle while preserving the reversible and dynamic nature that facilitates self-healing.[4,27,28]

Recently, we reported a successful approach taken toward photothermal therapy and near-infrared (NIR) imaging by using polymeric bilayer vesicles (polymersomes) as nanocarriers.[29] For this work, a unique molecular architecture was employed to design the amphiphiles that self-assemble into polymersomes. This molecular architecture is based on a linear dendritic structure that incorporates a generation three (G3) polyamidoamine (PAMAM) dendron as the hydrophilic dendritic block and a linear poly(caprolactone) (PCL) chain as the hydrophobic linear block.[29] This copolymer type is known as linear dendritic block copolymers (LDBCs).[30,31] The linear dendritic structure provides enhanced mechanical properties and results in monodispersed nanoparticles.[29,32−36] A library of LDBCs was synthesized by varying the hydrophobic to hydrophilic ratios. Morphological studies provided evidence of polymersomes above 70% hydrophobic wt % with approximate sizes ranging between 30 and 100 nm. These nanoparticles were successfully employed as a carrier to deliver a photothermal agent to living cells and execute photothermal-induced cell death. This study laid the foundation for our PCL−PAMAM LDBC nanoparticles to be utilized as nanocarriers in biomedical applications.[29]

https://doi.org/10.1021/acsapm.1c01131
ACS Appl. Polym. Mater. XXXX, XXX, XXX−XXX

Herein, we report a practical approach to enhance the stability and hydrophobic therapeutic loading efficiency of PCL−PAMAM LDBC nanoparticles via physical cross-linking. Pendant phenyl (Ph) groups were introduced to the PCL chains to generate $\pi-\pi$ interactions among PCL chains in the hydrophobic bilayer (Figure 1). On the basis of previous research in amphiphilic block copolymer self-assembly, an LDBC system consisting of 70% hydrophobic block wt % was selected for the study to yield polymersome-like nanoparticles.[29,37,38] By introducing different weight ratios of Ph substituents (5%, 10%, and 20% concerning the hydrophobic block wt %), a library of Ph substituted LDBCs was synthesized. After confirmation of the compositions, polymeric nanoparticles with internal cross-linking were formed in aqueous media by nanoprecipitation. The nanoparticles were then characterized by dynamic light scattering (DLS) and transmission electron microscopy (TEM) for the sizes and morphologies. Critical aggregation concentration (CAC) and hydrophobic loading efficiencies were calculated. Finally, in vitro photothermal activities were evaluated with selected hydrophobic photothermal agents, phenyl indolizine-C5 (C5) and indocyanine green (ICG).[39] Results were compared to our previously reported unsubstituted LDBCs (i.e., non-cross-linked nanoparticles) (70-PCL−PAMAM) shown in Figure S1.[29]

EXPERIMENTAL SECTION

Materials and Methods. Common solvents, HPLC solvents, and reagents were purchased from commercial suppliers (Sigma-Aldrich and Fisher Scientific) and used without additional purification. PAMAM-G3-Boc, 70-PCL-G3, and C5 were prepared as previously reported.[29,33,39] Indocyanine green (ICG) was purchased from Sigma-Aldrich. All synthetic procedures were carried out under ultrapurified nitrogen conditions, and standard Schlenk line techniques were employed unless otherwise specified. Chloroform (99.9%, Acros), chlorobenzene (99.8%, Sigma-Aldrich), and ε-caprolactone (99%, BTC) were distilled over CaH_2. Tin(II) 2-ethylhexanoate (Sn (Oct)$_2$, 92.5−100%, Sigma-Aldrich) was dried under vacuum (−100 kPa) for 5 days and stored in a glovebox (O_2 and H_2O < 0.1 ppm). PAMAM-G3Boc [the macroinitiator used for ring-opening polymerization (ROP)] and phenyl substituted ε-caprolactone (Ph-ε-CL) were freeze-dried before use. All of the weighing for the ROP was done in a glovebox. $^1H(^{13}C)$ NMR spectra were collected on a 300 or a 400 MHz spectrometer [Bruker Avance spectrometers (Bruker, Germany)]. Chemical shifts (δ) are denoted in parts per million (ppm) relative to an internal standard (tetramethylsilane; TMS) and referenced to a protonated solvent obtained from Cambridge Isotope Laboratories, Inc. ($CDCl_3$: δH 7.26 ppm, δC 77.16 ppm; MeOD: δH 3.31, 4.87 ppm). Abbreviations used are s (singlet), d (doublet), t (triplet), q (quartet), m (multiplet), and b (broad). Gel permeation chromatography (GPC) measurements were done using DMF, and measurements were done at a flow rate of 0.8 mL/min at 55 °C. A Shimadzu 20A GPC system equipped with two PSS GRAM analytical 100 Å columns and a differential refractive index detector was used. The data was evaluated using Astra 7.0 software. The GPC system was calibrated using poly(methyl methacrylate) (PMMA) standards. A JEOL 1230 TEM was used at 100 kV to obtain electron microscopy images using a bottom-mounted charge-coupled device (CCD) camera (Gatan Orius 831). TEM sample preparation and negative staining were done using a previously reported method.[29] HEK293 cells were cultured under standard conditions.[29]

Synthesis of Phenyl-ε-Caprolactone (Ph-ε-CL). Phenyl substituted ε-caprolactone was synthesized via Baeyer−Villiger oxidation of 4-phenylcyclohexanone.[40] As outlined in Scheme S1, 4-phenylcyclohexanone (200 mg, 1.15 mmol, 1.0 equiv) and benzoyl peroxide (741 mg, 2.30 mmol, 2.0 equiv) were dissolved in 5 mL of DCM. H_2O_2 (574 μL of a 60% solution in H_2O, 5.74 mmol, 5.0 equiv) was then added, and the mixture was stirred at room temperature for 16 h. Then, 100 mL of diethyl ether (Et_2O) was added to the resulting mixture and washed with sat. aq. Na_2SO_3 and sat. aq. $NaHCO_3$ (two washing cycles with 25 mL of each sat. aq. solution) and dried over anhydrous $MgSO_4$. The resulting solution was concentrated to 1 mL and directly loaded onto a silica column and eluted with a 10:1 hexanes/acetone mobile phase. Ph-ε-CL was obtained as white needle-like crystals (69.2% isolated yield).

Synthesis of PhPCL-G3. Phenyl substituted PCL−PAMAM (PhPCL-G3) LDBCs were synthesized by modifying a previously reported route.[29] A Boc protected generation three (G3) PAMAM dendron (PAMAM-G3Boc) was used to initiate the ROP of a mixture of ε-caprolactone and Ph-ε-CL by employing Sn(Oct)$_2$ as the catalyst. Different amounts (wt %) of Ph-ε-CL (5%, 10%, and 20% concerning hydrophobic block wt %) were introduced by varying the feed ratio for the Ph-ε-CL monomer while keeping the hydrophobic weight percent of the whole LDBC system constant (70% hydrophobic wt %, Table S1). The percentage of Ph-ε-CL was used to represent each system. For example, 10-PhPCL-G3 corresponds to an LDBC containing 10% of the hydrophobic block weight by PhPCL where the linear hydrophobic segment is a random polyester block copolymer via copolymerization of phenyl substituted ε-caprolactone and ε-caprolactone monomer. Trifluoroacetic acid (TFA) was used to remove the Boc protection of the terminal amine on the PAMAM block affording amphiphilicity.[29,32]

Characterization of Boc-Protected LDBC Precursors. The molar mass and the degree of polymerization (DP) were calculated using proton NMR spectra for all the precursors (i.e., before the Boc deprotection). Either MeOD or $CDCl_3$ was used as the solvent with TMS as the internal standard. GPC was utilized to confirm the molar masses calculated by NMR and obtain the dispersity ($Đ$) of the polymers. The NMR spectrum and GPC chromatograms are located in the Supporting Information.

Preparation and Characterization of Amphiphilic LDBCs and Their Self-Assembled Nanoparticles. After the Boc deprotection, the resulting LDBCs were analyzed by thermogravimetric analysis (TGA) and differential scanning calorimetry (DSC) to evaluate the thermal stability and qualitative compositions. For TGA, the TA Instruments TGA 55 was employed. A platinum pan was used for each sample, and the thermal studies were conducted under a nitrogen atmosphere within the temperature range of 25 to 500 °C at a ramp rate of 20 °C/min. For DSC, a TA Instruments DSCQ1000-0620 v9.9 was used. DSC scans were done at ramp rates of 20 °C/min with three heating/cooling cycles. The data were analyzed (for both TGA and DSC) using TA Instruments Universal Analysis 2000 4.5A software.

5-PhPCL-G3 and 10-PhPCL-G3 LDBC systems were formed into nanoparticles via a previously reported nanoprecipitation method.[29,32] 1 mg of LDBC was dissolved in THF (200 μL), and the resulting solution was added dropwise (1 drop/s) to a vial containing Milli-Q water (1 mL) while gently stirring and sonicating. THF was allowed to evaporate under constant airflow. Nanoformulations were allowed to equilibrate for 12 h before testing.

Particle size and zeta potential (ζ-potential) measurements were carried out on a Zetasizer Nano ZS (Malvern Instrument) using a He−Ne laser (633 nm) detector angle of 173° at 25 °C. The concentration was kept at 1 mg/mL for all the systems, and all measurements were done in triplicate to ensure consistency. Morphologies of the nanoparticles were obtained by environmental TEM and cryo-TEM.

The pyrene fluorescence probe method was carried out to obtain the CAC of the LDBC nanoparticles.[41,42] The experiment was carried out with a series of eight concentrations (10^{-8} to 10^{-1} mg/L). The fluorescence spectra were taken on a Varian Cary fluorescence spectrometer (Agilent Technologies). CAC was calculated by plotting the ratio of emission intensities at 338 and 333 nm as a function of the log of the concentration. Additional associative results are given in the Supporting Information.

Encapsulation Studies. Curcumin, indolizine cyanine C5,[39] and ICG were separately loaded into the nanoparticles. Chemical

https://doi.org/10.1021/acsapm.1c01131
ACS Appl. Polym. Mater. XXXX, XXX, XXX−XXX

structures, absorbance, and emission profiles for each dye are given in the Supporting Information. The encapsulation efficiency (EE%) and loading efficiency (DL%) were calculated for each dye using the following equations, where M_C = mass of the dye in the nanoparticle, M_P = mass of LDBC, and M_{Ci} = mass of the dye initially added.[43]

$$\text{DL}\ (\%) = 100 \times \frac{(M_C)}{(M_P + M_C)} \quad (1)$$

$$\text{EE}\ (\%) = 100 \times \frac{(M_C)}{(M_{Ci})} \quad (2)$$

A similar procedure was followed for all the dyes. One mg of dye and 2 mg of the block copolymer were dissolved in THF (200 μL). The nanoprecipitation method (vide supra) was followed to form dye-loaded nanoparticles. After the 12 h equilibrating period, the unloaded dye was filtered out using a 0.45 μm syringe filter. Water was then removed by freeze-drying. The resulting crude (dye-loaded nanoparticles) was redissolved in THF (5 mL) to solubilize the encapsulated dye. The amount of encapsulated dye was estimated using a Cary 6000 UV−visible spectrophotometer, and a standard calibration curve was obtained from free dye in THF.

Optical Activity of C5-Encapsulated Nanoparticles. Femtosecond transient absorption spectroscopy (fsTAS) was used to obtain the excited-state lifetimes for both C5 loaded nanoparticles and free C5. Optical pulses of a sub-100 fs bandwidth were generated using a Ti:sapphire regenerative amplified laser system (Coherent Astrella). The 800 nm fundamental output from the fs amplifier was tuned to the excitation wavelengths used for data acquisition inside an optical parametric amplifier (Light Conversion) before being routed into a transient absorption spectrometer (Ultrafast Systems Helios). Broadband probe pulses for measuring the transient absorption were generated inside the spectrometer by routing a portion of the 800 nm fs pulses through a CaF_2 crystal. The generation of the probe pulses in this manner preserves the temporal characteristics of the fundamental pulses, allowing for excellent resolution in time-resolved measurements and the detection of short-lived-transient species.[44]

Storage Stability of C5-Encapsulated Nanoparticles. Dynamic light scattering (DLS) was employed to evaluate the storage stability of C5-encapsulated nanoparticles. Dye-loaded nanoparticles were formed using the nanoprecipitation method explained in the encapsulation studies. Particle size and the PDI were then measured at 24 h intervals over 5 days and then 48 h intervals up to 10 days. Data collection was done using a Zetasizer Nano ZS (Malvern Instrument) using a He−Ne laser (633 nm) having a detector angle of 173° at 25 °C. The percent change in the size and PDI was plotted against the number of days to evaluate the stability.

Photothermal Efficiency.[45] The temperature increase of nanoparticle dispersions upon irradiation with an 808 nm laser was used to evaluate the photothermal efficiency. In a typical test, 2 mg LDBC prepared nanoparticles with photothermal agents were dispersed in 1 mL of Milli-Q water and placed in a 10 mm × 10 mm quartz cuvette. The dispersion temperature was monitored and allowed to equilibrate to room temperature. The dispersion was then irradiated with an 808 nm wavelength laser (1 W cm^{-2}) from the top of the liquid. The thermocouple inserted in the sample was kept out of the laser path, and the temperature was recorded every 10 s. The photothermal efficiency, η, was calculated by

$$\eta = \frac{hA(\Delta T_{max} - \Delta T_{sol})}{I(1 - 10^{-A_\lambda})}$$

where h is the heat transfer coefficient, A is the surface area of the container, ΔT_{max} is the maximum temperature change of the dispersion (this was obtained after the temperature ceased increasing and reached steady state), ΔT_{sol} is the maximum temperature change of Milli-Q water irradiated by the same laser, I is the laser irradiation power, and A_λ is the absorbance of the nanoparticles with photothermal agents loaded at 808 nm. The parameter set hA was determined by fitting temperature vs time during a naturally cooling process through this equation:

$$t = -\frac{\sum_i M_i c_{Pi}}{hA} \ln\left(\frac{\Delta T}{\Delta T_{max}}\right) \quad (3)$$

where t is the time since the cooling starts, M_i is the mass of component i in the system, c_{Pi} is the specific heat capacity of component i, and ΔT is the difference between liquid temperature and room temperature. $\sum_i M_i c_{Pi}$ is approximated by the mass and specific heat capacity of the Milli-Q water.

In Vitro Cell Uptake and Cytotoxicity Assay. Human embryonic kidney (HEK293) cells purchased from ATCC were used for the assay. HEK cells were grown under standard conditions (37 °C, 5% CO_2, DMEM media with 10% FBS). C5-encapsulated nanoparticles were added to tissue culture media and allowed a 24 h incubation period. LysoTracker Green DND-26 (Invitrogen) staining was performed to image lysosomes simultaneously. The distribution of dyes in the cells was visualized with a laser scanning confocal microscope (Zeiss LSM 510 META). Cytotoxicity of the nanoparticles (dye loaded and unloaded) was then evaluated with a CyQUANT LDH Cytotoxicity Assay Kit (Invitrogen) using a microplate reader (BioTek Synergy H1).

In Vitro Photothermal Assay. Human lung cancer (A549) cells were used for the assay. A549 cells were prepared in three 12-well plates and grown under standard conditions (37 °C, 5% CO_2, F-12K media with 10% FBS). A549 cells were washed with 10 mM PBS buffer and treated with 0 (A1, A2), 500 ng (A3, A4), 2.5 μg (B1, B2), 5 μg (B3, B4), 25 μg (C1, C2), and 50 μg (C3, C4) polymers in 1 mL of F-12K media. The cells were incubated overnight under 5% CO_2 at 37 °C. Then, one plate of cells was placed in the dark for 8 min, and the other two plates of cells were irradiated with the red LED of a commercial LED flood lamp (Novostella 100W RGB LED Flood Light), one for 8 min and one for 80 min, followed by incubation for 2 h. The light intensity was measured with a ThorLabs digital light meter (PM100D) and sensor (S120VC) and was found to be 9.7 ± 2.9 mW cm^{-2}. After incubation, the culture media of each well was removed and 200 or 10 mL of PBS buffer was added to each well. 200 mL of a LIVE/DEAD Cell Imaging assay solution was added in every well, and cell death was evaluated with a LIVE/DEAD Cell Imaging Kit (Invitrogen) following the manufacturer's protocols. Cell death was assessed as the percentage of dead cells by counting the live cells indicated by green fluorescence (GFP filter cube: 470/22 nm excitation, 525/50 nm emission) and the dead cells indicated by red fluorescence (RFP filter cube: 531/40 nm excitation, 593/40 nm emission) using an EVOS-fl fluorescence microscope. Two independent experiments were performed to ensure consistency. The statistical significance between the dark control and 8 min irradiation test and the statistical significance between the dark control and 80 min irradiation test were calculated using a two-tailed Student's t test with n = 4 technical replicates across two independent experiments.

RESULTS AND DISCUSSION

Design and Synthesis of Phenyl Substituted PCL−PAMAM LDBCs. In this work, we aim to increase the stability and hydrophobic therapeutic loading efficiency of the PCL−PAMAM LDBC nanoparticles. The potential of our nanoparticles to be utilized in photothermal therapy and NIR imaging has recently been proven using an unmodified LDBC, 70-PCL−PAMAM.[29,32] The linear dendritic structure and the selection of polymer types (i.e., PCL and PAMAM) focuses on the end-use of these nanoparticles as carriers in nanomedicine. PCL (hydrophobic block) is known for its excellent biocompatibility and is thus approved by the Food and Drug Administration (FDA) for safe practice in humans (e.g., surgical material containing PCL as a primary component). In contrast with other biocompatible polyesters, such as polylactides, PCL demonstrates an increased permeability toward hydrophobic therapeutic agents. The glass transition

https://doi.org/10.1021/acsapm.1c01131
ACS Appl. Polym. Mater. XXXX, XXX, XXX−XXX

Scheme 1. General Synthetic Route Towards PhPCL-G3 LDBCs[a]

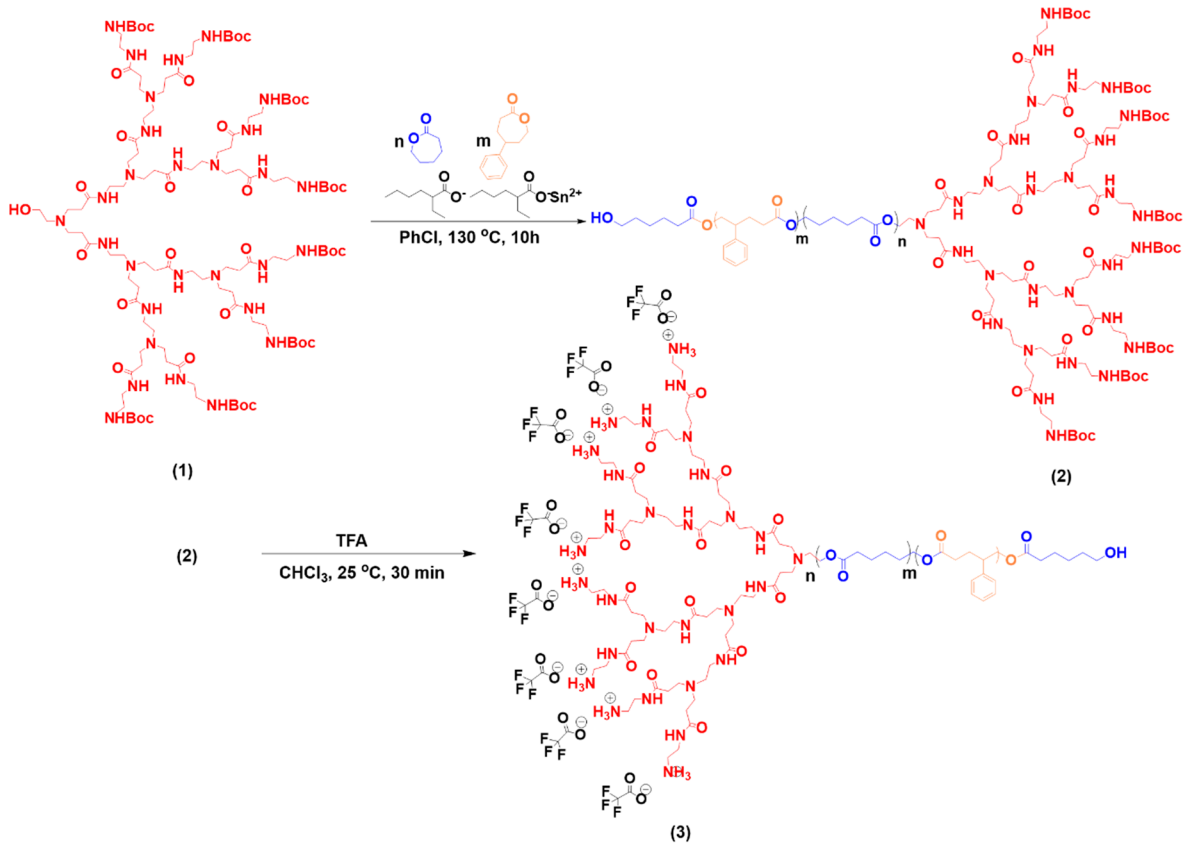

[a]Obtained by ROP of ε-caprolactone (blue) and Ph-ε-CL (orange) monomers initiated by the PAMAM-G3-Boc macroinitiator (1) to yield PhPCL-G3Boc (LDBC precursor) (2), which is then deprotected to obtain the final amphiphilic PhPCL-G3 LDBC (3).

temperature (T_g) for PCL is comparatively low (−60 °C), which adds a soft rubbery nature to the polymer matrix.[29,32,46−48] Furthermore, its lower acid degradation rate comes as an added advantage when designing nanocarriers for slow-release applications. The hydrophilic block, PAMAM, provides unique surface functionalities that can be strategically modified to achieve target-specific and stimuli-responsive carriers. Owing to its highly branched architecture, PAMAM can facilitate the transportation of a range of guest molecules via guest−host interactions.

Previous work has been reported on the introduction of benzyl and phenyl substitutions to PCL chains as a postmodification via alpha alkylation and click-chemistry (CuAAC and thiol-ene).[25,49] However, these approaches have setbacks due to the use of extreme reaction conditions (e.g., strong bases such as LDA), excessive synthetic and purification steps, and lack of synthetic feasibility to control the substituent amount. Furthermore, click approaches demand the addition of one reactant in excess to achieve good yields and require added steps to remove the excess reactants.[50,51] To overcome these challenges and control the substituent amount through a one-step synthesis, the caprolactone monomer was modified to achieve Ph-ε-CL prior to the ROP. Ph-ε-CL monomer was synthesized by the Baeyer−Villiger oxidation of 4-phenyl cyclohexanone (Scheme S1).

The synthetic approach employed here was designed to introduce pendant phenyl (Ph) groups to the linear PCL chain of the LDBC. We modified one of our previously reported syntheses to achieve a feasible synthetic strategy for this work (Scheme 1).[29] A Boc-protected G3 PAMAM dendron with an OH focal point (1) was used as the macroinitiator for the ROP of a mixture of ε-caprolactone and Ph-ε-CL monomers. By simply changing the ε-caprolactone to Ph-ε-CL feed ratio, we introduced different weight ratios (5%, 10%, and 20%) of pendant phenyl groups through a one-step and one-pot synthesis to yield a random hydrophobic polyester block attached to a hydrophilic PAMAM dendron. This synthetic strategy provides the simultaneous control of the phenyl substituent amount and the hydrophobic to hydrophilic weight ratios of the LDBC. The hydrophobic to hydrophilic wt % of the LDBC was kept constant (i.e., 70:30, PCL/PhPCL−PAMAM) regardless of the PhPCL wt %.

Although the $Sn(Oct)_2$ catalyst is known for its biocompatibility,[52] the catalyst concentration was kept at the minimum to avoid possible toxicity toward biological systems. Catalyst equivalents of 0.6 per hydroxyl focal point were identified as the optimal amount for 70-PCL-G3 and kept the same for the Ph-PCL series.[29] The percent conversions shown for the polymerization of 5-PhPCL and 10-PhPCL systems were above 93%. However, the 20-PhPCL system did not reach completion with the same catalyst amount (0.6 equiv). According to NMR evidence, the chain propagation was discontinued after adding 20 wt % of phenyl substituents. This indicates that the increased addition of phenyl groups to the growing polymer causes a depletion of the catalytic activity of $Sn(Oct)_2$. We speculate that, as more pendant phenyl groups are added to the propagating chain, several chains undergo aggregation via π−π interactions to form a bulky intermediate.

https://doi.org/10.1021/acsapm.1c01131
ACS Appl. Polym. Mater. XXXX, XXX, XXX−XXX

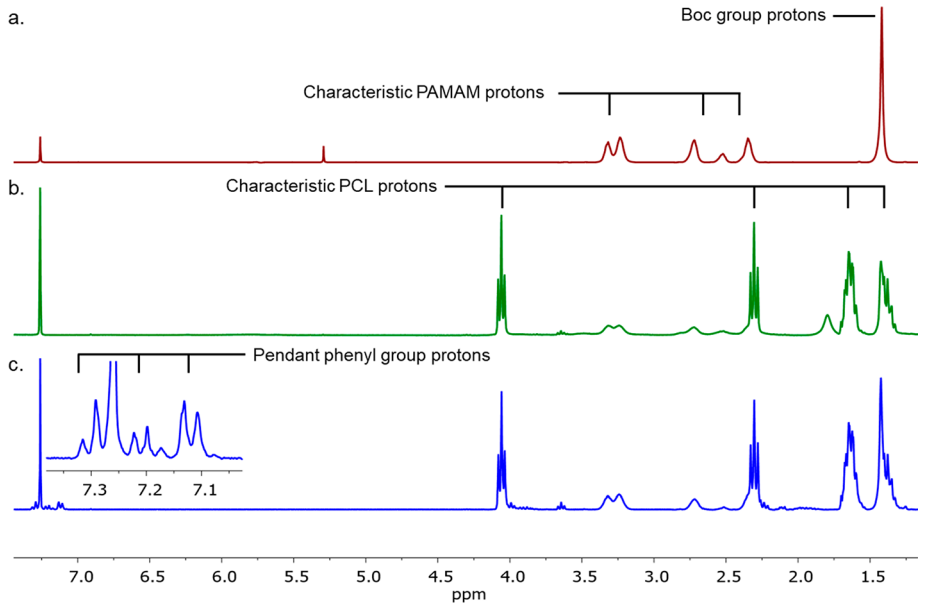

Figure 2. ^{1}H NMR overlay of the (a) macroinitiator (PAMAM-G3-Boc), (b) LDBC precursor (70-PhPCL-G3Boc), and (c) LDBC precursor (10-PhPCL-G3Boc) in $CDCl_3$.

This can disrupt the coordination among the propagating terminal, $Sn(Oct)_2$ catalyst, and monomer, resulting in chain growth termination. Additionally, we know from our previous works that the polymerization proceeds with a slow initiation and propagation with our PAMAM-G3Boc macroinitiator and can be further hindered with the addition of Ph-ε-CL monomer.[29,32] Therefore, we moved forward with 5-PhPCL and 10-PhPCL systems, and polymerization kinetic studies are being carried out with the focus on understanding the catalyst deactivation and termination of the chain growth under an increased Ph-ε-CL environment.

Molecular Weight Analysis of LDBCs. Molar mass characterization was done using NMR spectroscopy and GPC. The analysis was done with the Boc-protected LDBC precursors because of their better solubility in organic solvents. As the hydrophilic block (PAMAM-G3) is a constant for all the LDBCs, the characteristic peak at 3.30 ppm (with 46 protons) was used as the reference peak. The PCL peak at 4.05 ppm (methylene protons) was integrated with respect to the PAMAM reference peak to calculate the degree of polymerization of the hydrophobic chain (Figures S4 and S5, Table S2). The number of pendant phenyl groups was calculated using the aromatic resonance signals between 7.05 and 7.35 ppm (Figure 2c). Molar mass data obtained from GPC agrees with the calculated molar mass values from NMR (Table S2). The chromatographic behavior (Figure S6) of the linear dendritic architecture is presumably a result of a delayed or slow initiation and propagation with the PAMAM-G3Boc macroinitiator.[29,32,53,54] According to the previous kinetic studies,[29,32] an increase in the catalytic equivalents causes an increase in initiation time. However, we have kept the catalytic equivalents low despite a compromise to the dispersity of the resulting polymer. Furthermore, it is known that intermolecular ester interchange occurs at high temperatures. As the ROP was carried out at 130 °C, this ester interchange is possible until the most abundant molar mass distribution is established.[38,55] This may lead to broad molar mass distributions that result in a higher $Đ$.[38] However, with the synthetic approach taken in this work, $Đ$ values did not exceed 1.3, which is a favorable trend. NMR spectra and GPC chromatograms are given in the Supporting Information.

Amphiphile Formation. The ^{1}H NMR spectra overlay of PAMAM-G3Boc, 70-CL-G3Boc, and 10-PhPCL-G3Boc (Figure 2) illustrates the characteristic signals along with the incorporation of the macroinitiator to the phenyl substituted LDBC system. Resonance peaks corresponding to the Boc-protected macroinitiator (2.19−3.69 ppm) and the LDBC with no phenyl substituents (70-CL-G3Boc; 1.38, 1.64, 2.30, and 4.05 ppm) are shown in Figure 2a,b, respectively. Figure 2c represents 10-PhPCL-G3Boc, the LDBC precursor with pendant phenyl substituents (10% of the hydrophobic weight), while maintaining the overall 70:30 hydrophobic to hydrophilic weight ratio. After the Boc deprotection, the intensities of PAMAM resonance peaks decreased dramatically (Figure S3) in $CDCl_3$. This observation was expected, and similar results were observed with the previously reported LDBCs.[29] The deprotection decreases the solubility of PAMAM in organic solvents, which leads to solvent-driven self-assembly. As the self-assembly occurs in an organic solvent, more soluble PCL forms the outer corona of the nanoparticle while less soluble PAMAM stays shielded in the core. This is described as reverse-phase nanoaggregation. Due to the phase change experienced by the PAMAM in the nanoparticle, a change in relaxation time occurs and suppresses signal intensities corresponding to PAMAM in the ^{1}H NMR spectrum.

Thermal Analysis. Thermal properties of the PhPCL-G3 LDBC series were evaluated using TGA/DTG and DSC. Boc deprotected amphiphilic LDBCs (containing NH_3^+ end groups) were used for the analysis. TGA/DTG is a well-known and convenient method to deduce relative compositions of block copolymers qualitatively.[38,56] By analyzing the weight loss percentage (ΔW) and the inflection point temperature (T_d) related to each block, a qualitative calculation of the decomposition temperatures and the weight percent of the blocks was carried out.

As the polymers consist of three different components (PAMAM, PCL, and PhPCL), three different thermal degradation events were expected (Table S3). The thermo-

https://doi.org/10.1021/acsapm.1c01131
ACS Appl. Polym. Mater. XXXX, XXX, XXX−XXX

gram of the 10-PhPCL-G3 system (Figure 3, Table S3) showed concurrence with the theoretical assumption by giving

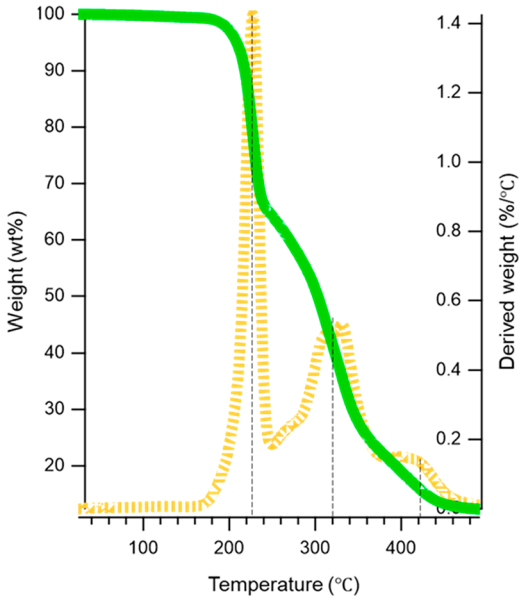

Figure 3. TGA (green) and derived thermogravimetry (DTG) (yellow) thermograms for 10-PhPCL-G3 under nitrogen. Vertical dotted lines indicate T_d for major thermal degradation events.

inflection point temperatures at 226, 321, and 422 °C. The T_d and ΔW values (Table S3) correlate well with the degradation of the hydrophilic block (PAMAM, Figure S7).[29] The theoretical PAMAM ratio in the block copolymer is 30%, which qualitatively aligns with the ΔW percentage obtained for the first degradation step (32.5%) observed in TGA (Figure S9). The latter decompositions summing up to 67.5% represent the hydrophobic block (PCL and PhPCL) that contains 70% of the weight theoretically. According to the inflection point temperatures reported in the literature, T_d at 321 °C represents the decomposition of PCL.[29] Furthermore, the thermograms reported for our previous LDBC, 70-PCL-G3, did not show the decomposition at 422 °C (Figure S11).[29] This suggests that the final thermal event is related to the decomposition of phenyl substituents on the PCL chain (Figures 3 and S8−S11). For the 10-PhPCL-G3 system, PhPCL takes 10% of the hydrophobic weight, which is 7% of the total weight of the block copolymer. The ΔW percentage of the final thermal event is approximately 8%, providing additional evidence for the decomposition of pendant phenyl groups. The correlations between the weight ratio of each block, composition, T_d, and ΔW at each thermal degradation event support the reliability of the synthetic methodology developed for this work. Similar results were seen with 5-PhPCL-G3 (Figures S8 and S10). However, the decomposition step for the PhPCL units was not prominent enough to conduct a reliable calculation. The lower PhPCL content in 5-PhPCL-G3 is the most probable reason for this observation. Additional TGA data as well as predicted and experimental compositions are included in Table S3 and Figures S7−S11.

Unlike previous studies,[29,32] no obvious thermal features were observed in the DSC thermograms for both polymeric series. The melting temperature (T_m) range and glass transition temperature (T_g) for pure PCL are reported as 59−64 and −60 °C, respectively. For our previous LDBCs that consist of a polyester block above 90 wt %, sharp and intense thermal events were reported.[29] In those studies, when the hydrophobic wt % decreases, changes in the peak shape (from sharp and intense to broad) were observed as the PAMAM block. For this polymer series, the substituents (i.e., phenyl) were expected to strongly affect the thermal properties of PCL at lower PCL weight ratios. However, the thermograms shown in Figures S12 and S13 appear broad and featureless, demonstrating the influence of substituents on the properties of the PCL block as this was not seen for the thermograms of 70-PCL-G3.[29] The lack of clear melting transition peaks can arise as a result of the poor crystallinity of the polymer due to the random distribution of phenyl groups in the linear block and the influence of the dendritic block. Such deviations are well-known for low molecular weight block copolymers and point to the contribution of substituents to the thermal properties of the polymeric system.[57]

Critical Aggregation Concentration (CAC) and Self-Assembly. As previously stated, the low stability of the nanocarrier in the systemic circulation is a significant bottleneck regarding the development of efficient nanoparticle-based delivery systems. Many different factors govern the stability of the nanoparticle, including surface charge, polymer concentration, the molar mass of the block responsible for the core formation, and the loaded host molecules.[58] Here, the surface charges, expressed as ζ-potential, for the nanoparticles formed by PhPCL-G3 were all positive with values of 51.2 ± 0.47 mV for 5-PhPCL-G3 and 66.4 ± 10.3 mV for 10-PhPCL-G3. Such values are due to the hydrophilic block containing a cationic terminus and making up the outer corona of the nanoparticle. Although concerningly high for biomaterials, these values are indicative of stable colloidal structures.[59,60]

The polymer concentration is a crucial parameter when forming nanoparticles. The CAC denotes the minimum polymer concentration needed to form self-assembled nanoparticles in a particular medium. A dilution below the CAC leads the nanoparticles to disintegrate/disassemble rapidly.[58,61] The magnitude of the CAC primarily depends on the size and hydrophobicity of the block that makes the core. Thereby, when the molar mass and the hydrophobicity of the polyester block are increased, the CAC can be decreased.[62] However, an increase in the hydrophobic molar mass has limitations because the block copolymer should maintain a particular hydrophobic/hydrophilic weight ratio to form biocompatible morphologies and sizes.[58,63,64]

Here, we sought to use phenyl groups to stabilize the nanoparticles without affecting the molar masses of the blocks. Additionally, the nanoparticles are stabilized not only by making cross-links but also by increasing the hydrophobicity of the core-forming block. The CAC for 5-PhPCL-G3 was 6.17 mg/L, which does not show a notable decrease relative to LDBCs with no phenyl groups (70-PCL-G3, 6.20 mg/L). In contrast, the CAC for the 10-PhPCL-G3 nanoparticles showed a 37.1% relative decrease of the CAC (3.90 mg/L) obtained for 70-PCL-G3. This reflects the effect of both increased hydrophobicity and $\pi-\pi$ cross-linking on the aggregation behavior of the nanoparticle. Nanoparticles with low CAC values resist disintegration upon a more extensive dilution. Such systems can tolerate a higher degree of dilution (such as bloodstream dilution), making the nanocarriers more stable in biological systems. Furthermore, physical cross-linking can reform the particle even after a disintegration, which is known

https://doi.org/10.1021/acsapm.1c01131
ACS Appl. Polym. Mater. XXXX, XXX, XXX−XXX

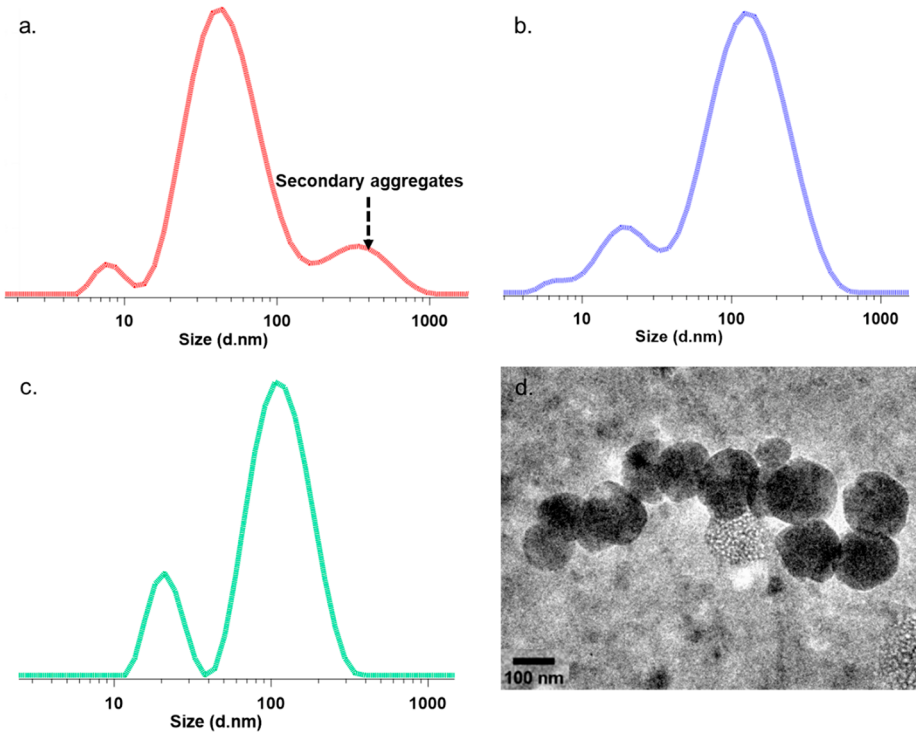

Figure 4. Intensity average DLS size distribution plots for (a) 70-PCL-G3 (LDBC system with no Ph substituents), (b) 5-PhPCL-G3, (c) 10-PhPCL-G3, and (d) morphology of 10-PhPCL-G3 nanoparticles under cryo-TEM.

as self-healing.[17,18] Supporting data for the CAC are included in Figure S14.

For the size and morphological analysis, nanoparticles were formed in water by conventional nanoprecipitation. The size distributions and dispersity of the nanoparticles in the solution were determined using DLS (Figure 4). Nanoparticles formed from 5-PhPCL-G3 exhibited a *Z*-avg particle size of 78.6 nm and a PDI of 0.53 with intensity and number averages of 204.2 and 10.4 nm, respectively (Figures 4b and S15−S17). Of particular interest are the nanoparticles formed from the PhPCL-G3 LDBC self-assembly. The *Z*-avg particle size for 10-PhPCL-G3 LDBC nanoparticles was 74.4 nm, which was represented by two major size distributions. According to the intensity average scattering plots, one distribution was around 130.6 nm and the other distribution, around 18.3 nm (Figure 4c). The existence of these distributions for 10-PhPCL-G3 LDBC nanoparticles was supported by number and volume average plots as well (Figures S18−S20). The dispersity (PDI) of these nanoparticle suspensions was 0.45, which is typical for a nanoparticle dispersion with several size distributions. Additional supporting data for 10-PhPCL-G3 LDBC nanoparticle sizes and morphologies were collected via transmission electron microscopy (TEM; Figures 4d and S21). The average diameter calculated for TEM images was 127.0 nm, which agrees with the hydrodynamic diameter of the main size distribution obtained by DLS. A TEM contrasting agent, uranyl formate, was utilized to observe the areas with different densities in the nanoparticles. Two distinct regions in the nanoparticles showed a distinctive contrast difference providing indirect evidence for bilayer vesicle morphology (Figure S21).

When comparing these results with the size distributions of the unsubstituted LDBC (70-PCL-G3),[29] an increase in particle size was observed. The phenyl substituents increase the volume of the hydrophobic block, which could lead to a volume expansion of the hydrophobic core, thereby increasing the size of the nanoparticles. Other than the major size distributions, larger secondary aggregates (clusters formed by smaller nanoparticles) were observed for the 70-PCL-G3 system (Figure 4a). The formation of secondary aggregates results from the fusion of smaller nanoparticles to reduce their excess surface energy.[29,65−67] The probable cause for this observation is the reduced surface energy of the nanoparticles due to the size expansion (Figure 4b). Additional DLS data is included in Figures S15−S20.

According to the literature, copolymers with hydrophobic weight ratios of ≥70 wt % self-assembled into bilayer vesicles (polymersomes).[4,29] This can also be justified by the principles of self-assembly. Israelachvili et al.[64] showed that morphologies and the curvature could be predicted using the packing parameter (p) given in eq 4, where ν is the hydrophobic volume, a_0 is the optimal area of the head (hydrophilic block), and L_c is the length of the hydrophobic block.

$$p = \frac{\nu}{a_0 L_c} \tag{4}$$

The hydrophilic area (a_0) is not a variable for the LDBCs discussed in this work because a G3 PAMAM dendron is a constant throughout the series. Therefore, the hydrophobic block volume and the weight percentage are the driving forces to achieve different curvatures that define p. According to the theory, p should be between 1/2 and 1 to form vesicles. In turn, it is logical to deduce that the spherical nanoparticles observed here possess bilayer vesicle (polymersome) morphologies, further supported by the TEM images (Figure S21).

Preliminary Encapsulation Studies. In order to identify the optimal phenyl substituent percentage to enhance the hydrophobic loading ability, the DL% of each PhPCL-G3

https://doi.org/10.1021/acsapm.1c01131
ACS Appl. Polym. Mater. XXXX, XXX, XXX−XXX

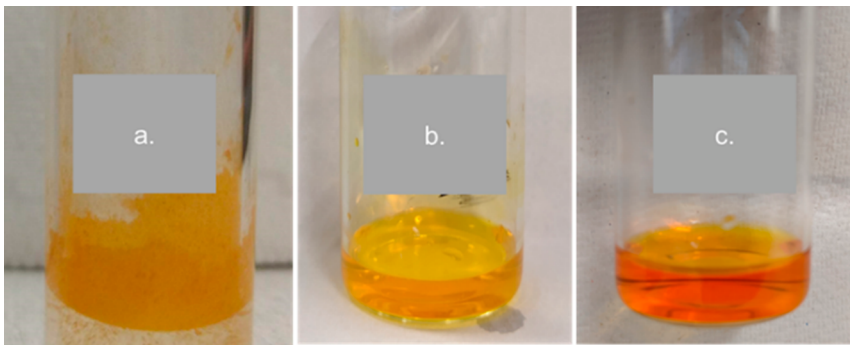

Figure 5. (a) Dispersion of curcumin in water, (b) curcumin-loaded 5-PhPCL-G3, (c) curcumin-loaded 10-PhPCL-G3.

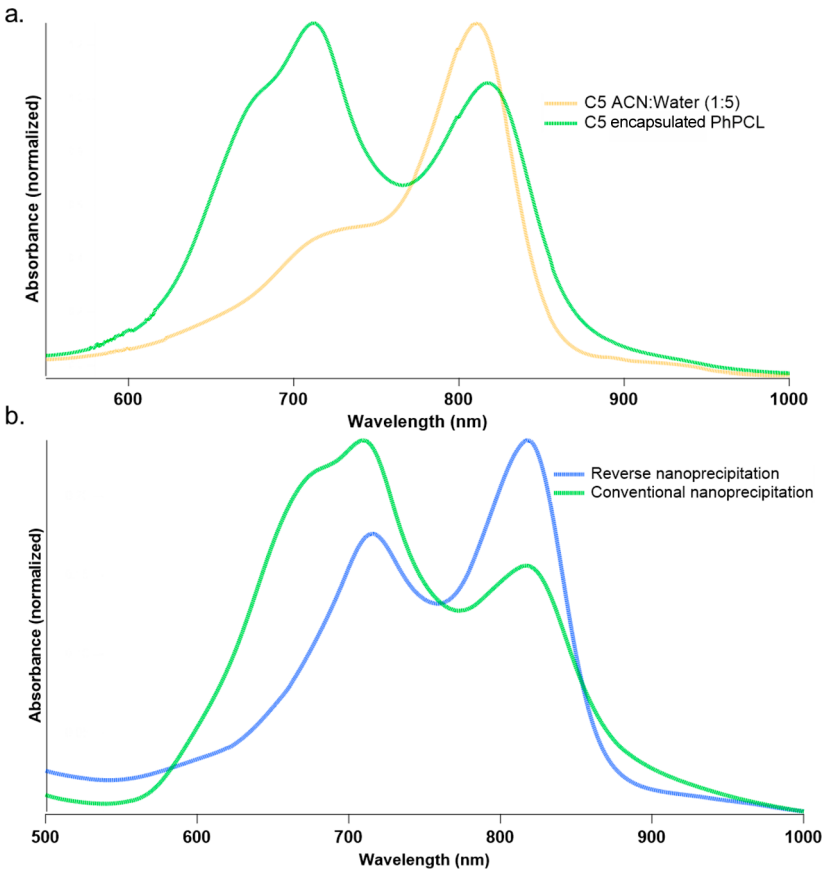

Figure 6. (a) Absorption spectra of free C5 (dissolved in a 1:5 ACN/water mixture) and the encapsulated C5 in 10-PhPCL LDBC nanoparticles; (b) absorption spectra of C5 encapsulated by conventional nanoprecipitation and reverse nanoprecipitation.

LDBC was compared with that of 70-PCL-G3. The studies were initiated with curcumin, a hydrophobic molecule (chemically referred to as diferuloylmethane).[68] The high hydrophobicity and the ease of detection (UV−vis spectroscopy) inherited from curcumin were employed to observe the changes in hydrophobic loading profiles. As phenyl groups are present in the hydrophobic bilayer, we hypothesized that the phenyl substituted LDBCs would increase the uptake of curcumin via enhanced $\pi-\pi$ interactions. Both 5- and 10-PhPCL-G3 dramatically increased the water solubility of curcumin (Figure 5b,c) via nanoparticle encapsulation. Without the presence of LDBC nanoparticles, the dye was completely insoluble in water, forming a separate layer on the water surface and the vial walls (Figure 5a). The reported DL% for 70-PCL-G3 is 13.70%.[29] The DL% of curcumin into the 5-PhPCL-G3 nanoparticles was 13.73%, which is not a significant increase compared to the nonphenylated LDBC.[29] However, the 10-PhPCL-G3 LDBC shows a DL% of 17.50, which is a 27.7% relative increase in the loading efficiency toward a hydrophobic guest molecule.

The preliminary encapsulation studies with curcumin suggest that the introduction of 5 wt % phenyl substituents is insufficient for significantly enhancing hydrophobic loading efficiency. On the other hand, the increase of the substituent wt % up to 10% demonstrated a notable enhancement in the loading efficiency. Similar results were observed with several other selected hydrophobic molecules (Table S4).

Although the hydrophobic interactions are a primary driving force determining the loading efficiency, the miscibility between polymers and the host molecule is another vital fact

https://doi.org/10.1021/acsapm.1c01131
ACS Appl. Polym. Mater. XXXX, XXX, XXX−XXX

to be considered. The loading basically refers to the mixing between the hydrophobic polymer and the drug. This can be explained by the Flory–Huggins equation (eq 5)

$$X_{\text{polymer-drug}} = (V_{\text{drug}}/RT)(\delta_{\text{drug}} - \delta_{\text{polymer}}) \quad (5)$$

where X is the Flory–Huggins parameter for the interactions between the drug and the polymer, V_{drug} is the volume of the drug, δ is the Hildebrand–Scatchard solubility parameter, and R and T are the gas constant and the temperature, respectively. δ is a factor related to the drug loading of a polymeric micelle.[29,58,61,69] Using this relationship, Liu et al. examined the miscibility of different hydrophobic molecules (curcumin, paclitaxel, plumbagin, indomethacin, and etoposide) with PEG–PCL nanoparticles.[61,70] Surprisingly, they observed that the best solubility (loading) is for indomethacin, one of the least hydrophobic molecule in the series. Another study carried out with different polymeric backbones showed the loading is related to the heat of the mixing. The observed trend was poly(benzyl-L-aspartate) (PBLA) > PCL > polylactide (PLA) > polyglycolide (PGA).[70] This observation suggests that PCL has a better mixing ability toward hydrophobic drugs, which rationalizes the polymeric material selection for this work. Also, it is important to note that the heat of the mixing related to the polymer type is another factor that affects the loading. Consequently, the results observed for the loading ability of PhPCL-G3 nanoparticles may be varied according to the drug molecule and the selection of polymer types.

Photothermal Efficiency. As 5-PhPCL-G3 LDBC nanoparticles did not display significantly increased loading efficiencies and decreased CAC values, the remaining studies were carried out with 10-PhPCL-G3 LDBCs.

There have been reported attempts of utilizing cyanine-based photothermal imaging agents to showcase the theranostic potential of LDBC nanoparticles.[29] These dyes are known for their photoacoustic imaging applications (PAI) and near-infrared fluorescence (NIRF) imaging. In addition, they can transform absorbed NIR photons to heat, which makes them useful in photothermal therapy. However, the hydrophobicity and instability in the aqueous medium have hindered their full potential to be used as photothermal and imaging agents in biological systems. Herein, we focus on enhancing the water solubility of selected hydrophobic cyanine dyes and evaluate their potential in photothermal therapy and NIR-imaging. Phenyl indolizine-C5 or C5, a recently reported near-infrared (NIR) emissive cyanine dye, was chosen for these studies.[39] The dye is insoluble in water, but encapsulation in LDBCs made it highly soluble in water (Figure 6). Upon uptake of C5, we saw a decrease in PDI as well as an ∼70 nm increase in size. The DL% obtained for 70-PCL-G3 (no phenyl substituents) was 2.58%. Interestingly, C5 loading using the phenyl substituted LDBCs exhibited an enhanced loading efficiency of 32.1%. Although the comparative increase of DL% of C5 is significant, the DL% values are considerably lower than that of curcumin (Table S4). As both C3 and C5 are indolizine–cyanine salts, they could possess a diminished hydrophobicity and their partitioning coefficient can cause the observed lower DL% compared to curcumin.

"Free" (nonencapsulated) C5 in a solution of ACN and H_2O (1:5) gave a low-energy absorbance maximum wavelength ($\lambda_{\text{abs}}^{\text{max}}$) and emission maxima ($\lambda_{\text{emis}}^{\text{max}}$) of 810 and 826 nm, respectively (Figures 6 and S22). However, after the encapsulation of C5 in LDBC nanoparticles, a prominent high energy absorption peak at ∼700 nm appears (Figure 6a) in addition to its characteristic low energy absorption band (810 nm), a similar peak observed for the nonencapsulated form. When comparing the two spectra, the significant intensity increase at 705 nm indicates the presence of an aggregated state for the cyanine dye.[39,71] This suggests that the dye exists in the nanoparticle in two different states. The low energy absorption represents the dispersed C5 (which mimics that of the "free" dye in organic solvent or the nonencapsulated form). The newly appeared high-energy absorbance is indicative of an H-aggregated formation. H-aggregates are common organizational states for cyanine dyes and result from the face-to-face interactions of the dye framework. The appearance of H-aggregates after the encapsulation suggests that these LDBC nanoparticles force the dye molecules to form face-to-face interactions rather than head-to-tail interactions. In order to obtain more supporting evidence for the presence of H-aggregates, emission spectra were studied (Figures S22 and S23). As H-aggregates often inherit a poor emissive behavior due to the excited-state to ground-state radiative transition being forbidden by symmetry,[72] one should observe emission solely from the monomeric or "free" form of the dye dispersed in the nanoparticle ($\lambda_{\text{max}}^{\text{abs}}$ = 810 nm). When comparing the emission spectra of the "free" (in solution) and the encapsulated dye, a similar emission ($\lambda_{\text{max}}^{\text{ems}}$ = 826 nm) was observed for both forms regardless of the excitation wavelength (700 and 810 nm). This indicates the emission of the encapsulated state is from the monomeric form (i.e., dispersed C5 in the nanoparticle) but not from potential H-aggregates. Additionally, we observed a change in the peak intensity ratio (possible H-aggregates/dispersed) over a three-day time period from the day of encapsulation (Figure S23). The absorption peak intensity ratio was 1.3:1 (possible H-aggregates/dispersed) 12 h after the encapsulation. The ratio became approximately 1:1 after 48 h and remained the same ratio after 3 days (Figure S23), indicating a dynamic equilibrium between the aggregated form and the monomeric/dispersed form. We were able to shift this equilibrium more toward dispersed C5 by changing the nanoformulation method from conventional nanoprecipitation to reverse nanoprecipitation (Figure 6b). Additionally, we observed a difference in absorbance intensity. Conventional nanoprecipitation showed an overall higher intensity than reverse nanoprecipitation, which gives an indirect indication that DL % for the latter is less than the former. These eminent observations suggest that the aggregation behavior of the dye inside the nanoparticles can be controlled according to the need. Further studies are being carried out to understand more about these aggregation behaviors and the possibilities of J-aggregate formation.

The excited-state lifetime (τ) was evaluated before and after encapsulation (Figure S24). The "free" form of C5 in solution (1:1 ACN, H_2O) decays with a single exponential and a lifetime of about 45.7 ps. The encapsulated molecule shows double exponential decay with a fast component of around 1.36 ps and a slow component at 8.91 ps. These two components could be a result of the different aggregation behaviors discussed above. The calculated photothermal efficiency (η) for C5 encapsulated PhPCL-G3 nanoparticles was 49.4%. In order to benchmark the obtained results, an FDA-approved commercially available photothermal agent, indocyanine green (ICG), was used. The photothermal efficiency for ICG encapsulated nanoparticles was 47.2% (Table S5), demonstrating the potential of C5 loaded LDBC

https://doi.org/10.1021/acsapm.1c01131
ACS Appl. Polym. Mater. XXXX, XXX, XXX–XXX

nanoparticles as a photothermal agent. Upon the irradiation with a NIR laser, these nanoparticles were able to increase the temperature of the system from 21.6 to 66 °C in 20 min, which is comparable with the values observed for the ICG loaded nanoparticles (Figure 7c).

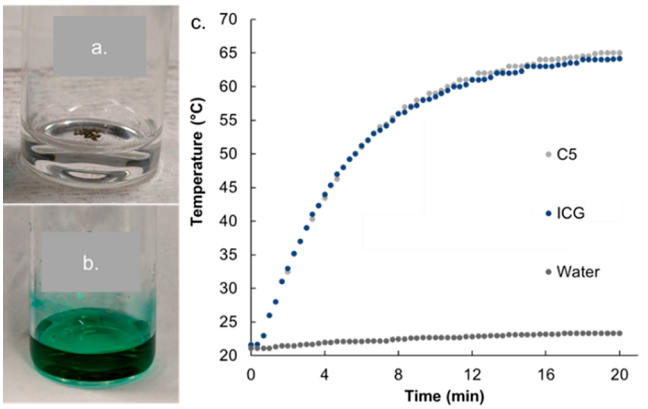

Figure 7. (a) Dispersion of C5 in water; (b) C5 loaded 10-PhPCL-G3; (c) photothermal activity of the PhPCL-G3 nanoparticles.

When looking at the storage lifetimes, the 10-PhPCL-G3 nanoparticles showed a 2-fold increase compared to 70-PCL-G3 with a loaded hydrophobic agent. 70-PCL-G3 nanoparticles started showing significant size and PDI changes after 5 days upon the encapsulation.[29] Interestingly, PhPCL-G3 nanoparticles managed to achieve and retain a PDI closer to 0.1 even after 10 days of encapsulation. There were no observed visual changes (i.e., no color change or precipitate formation) and significant changes in the size of the distributions (Table S6). These results signify that nanoparticles formed from PhPCL-G3 can maintain highly monodispersed particle suspensions even with a loaded hydrophobic agent for more than 10 days. These extended storage lifetimes were obtained without any specific preservation protocol such as PEGylation or lyophilization; thus, these lifetimes are exceptional for biomedical application where storage shelf lives in solution form are needed. Furthermore, these lifetimes are well comparable with the reported values for cargo-loaded nanoparticles having similar morphologies.[72−74]

Nanoparticles in Biological Imaging and Phototherapy. The cytotoxicity of C5-loaded nanoparticles and the empty nanoparticles (no loaded dye) was tested with HEK293 cells. Despite highly positive ζ-potentials, empty nanoparticles showed ≥97% cell viability for all the concentrations (Figure 8), while the observed cell viability for C5-loaded nanoparticles was ≥87.5%. Although highly cationic charge densities have been reported to induce cell lysis,[75] the most logical explanation for the observed cell viabilities is that the surface charge decreases due to nonspecific plasma protein adsorption onto the nanoparticle surface.[76,77]

The most significant impact on cell viability was seen with C5-loaded 10-PhPCL-G3, even more so than with C5 loaded 70-PCL-G3 where no cross-linking is present. This suggests a modest cost associated with the stability offered by cross-linking. In this case, cellular enzymes could be confounded by cross-linking, leading to a persistent release of dye and a subsequent increased impact on cell viability. Nonetheless, even at the highest concentration tested (50 μg/mL), both dye-loaded and empty nanoparticles exhibit generally minimal cytotoxicity.

The fluorescence of C5-loaded nanoparticles was imaged after uptake by HEK293 cells (Figure 8b). In live cell culture, particles appear to load through filopodial processes, a route seen for polyplexes such as those generated from glycopolymers[78] and other PAMAM-based nanoparticles.[79] Similar to these polymer systems, nanoparticles are trafficked to lysosomal compartments (Figure 8c−e) as observed using LysoTracker (green) to image lysosomes alongside fluorescence associated with the C5 dye. Co-localization was confirmed by calculating the Pearson coefficient, 0.6313 at a 41.65% colocalization rate (Figure 8c). Together, this suggests that the dye-loaded nanoparticles traffic through endosomes after being taken up by the cells and ultimately accumulate in the lysosomes.[29]

The phototherapeutic efficiency of C5-loaded nanoparticles was evaluated in human lung cancer (A549) cells. Two independent sets of experiments were performed where cells

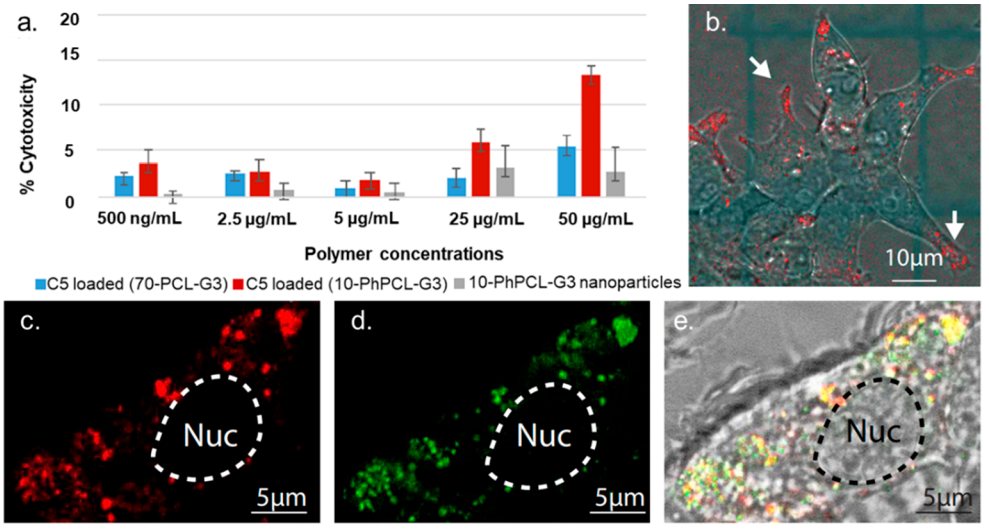

Figure 8. (a) Cytotoxicity (percentage) was determined by the LDH assay; (b) HEK293 cells after exposure to dye-loaded nanoparticles; (c) C5 dye fluorescence alone (red) in HEK293 cells; (d) LysoTracker fluorescence (green); (e) a merge of the bright field with LysoTracker and C5.

https://doi.org/10.1021/acsapm.1c01131
ACS Appl. Polym. Mater. XXXX, XXX, XXX−XXX

treated with varying concentrations of the nanoparticle suspension were irradiated with a 100 W red LED lamp for 0, 8, or 80 min (Figures S25 and S26). Concentration dependent studies aligned well with cell viability data demonstrating an effective dosage of 5 μg/mL. Figure 9

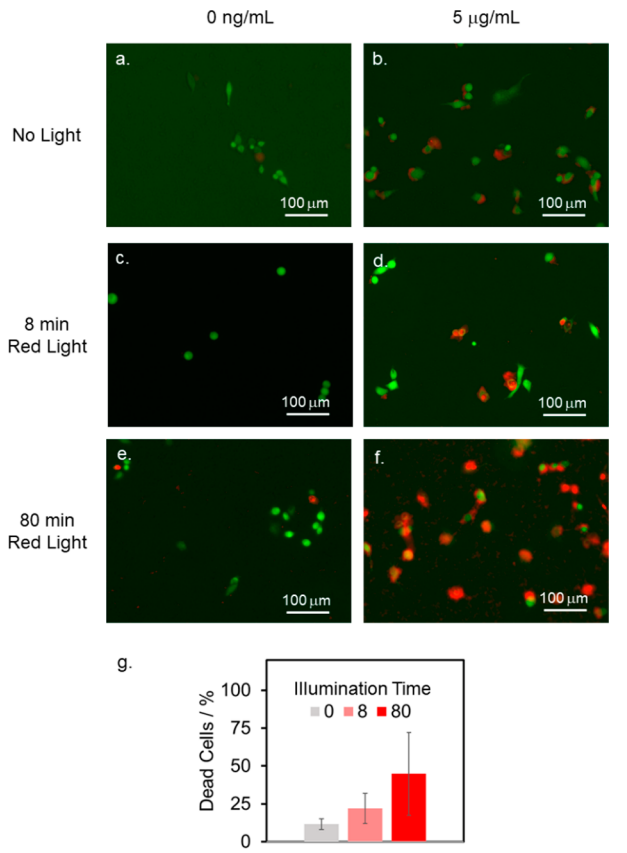

Figure 9. (a–f) Overlay of fluorescence images of A549 cells imaged using a LIVE/DEAD assay. Controls, with no nanoparticle loading (a, c, e); C5-loaded nanoparticles formed from 10-PhPCL-G3 with human lung cancer (A549) cells without (b) and after 8 min (d) or 80 min (f) of red light exposure. (g) Cell death count before and after light exposure with and without nanoparticles. Error bars are ± SD of n = 4 technical replicates across 2 independent experiments.

summarizes the in vitro photothermal assessment of cancer cells treated with C5-loaded nanoparticles with and without red light exposure. Compared to cells treated with no dye-loaded nanoparticle or light irradiation alone (Figure 9a,c,e), results indicate an increase in cell death is achieved after irradiation (Figure 9d) and enhances with time (Figure 9f). Figure 9g quantifies the difference in the number of dead cells relative to nanoparticle treatment and irradiation time, showing a clear trend with increasing illumination time. These results provide promising evidence for the use of these LDBCs and their dye-loaded nanoparticles as theranostic agents.

CONCLUSIONS

This work presents a successful attempt to enhance the hydrophobic loading efficiency and mechanical stability of LDBC nanoparticles by introducing cross-linking. Noncovalent cross-linking was made via π–π stacking in the polyester segment of polymeric nanoparticles. A ε-caprolactone monomer was modified via a phenyl substitution, and different weight ratios (5% and 10% concerning the hydrophobic block) were introduced into the linear hydrophobic block of newly designed LDBCs. In addition to the conventional structural characterization with NMR and GPC, TGA/DTG provided qualitative evidence for the reliability of the synthetic strategy employed. In comparison to an LDBC system with no phenyl substituents, a 37.1% decrease in the CAC was observed, indicating an enhanced stability due to increased hydrophobicity of the polyester block and core-cross-linking in the nanoparticles. Preliminary encapsulation studies showed a 27.3–41.2% relative increase of hydrophobic loading efficiency toward selected hydrophobic guest molecules. A near-infrared (NIR) emissive cyanine dye C5 was successfully loaded into these LDBC nanoparticles, and the photothermal efficiency was compared with ICG. C5 loaded nanocarriers showed a photothermal efficiency of 49.4%, which is similar to the efficacy of ICG (47.2%). Furthermore, C5-loaded LDBC nanoparticles increased the temperature from 21.6 to 66 °C after 20 min of photothermal activity. C5-loaded nanoparticles were successfully trafficked into HEK293 cells with no significant toxicity. Uptake was seen to proceed through a filopodia process via an endosome route with final accumulation in the lysosomes.

Upon exposure to red light irradiation, C5-loaded nanoparticles were able to induce cell death in cancer cells. This work highlights the effects of aromatic functionalization on the self-assembly and encapsulation properties of the LDBC nanoparticles. The enhanced colloidal stability, hydrophobic loading, and photothermal activity suggest that the physical cross-linking improves the potential of LDBCs in theranostic applications. The next level of this work will be focusing on understanding the aggregation behaviors of hydrophobic imaging/photothermal agents in LDBC nanoparticles and selective H-aggregate and J-aggregate formation according to the application perspective.

ASSOCIATED CONTENT

Supporting Information

The Supporting Information is available free of charge at https://pubs.acs.org/doi/10.1021/acsapm.1c01131.

Additional synthesis procedures, spectroscopic analysis, and photothermal experiments (PDF)

AUTHOR INFORMATION

Corresponding Author

Davita L. Watkins – *Department of Chemistry and Biochemistry, University of Mississippi, University, Mississippi 38677, United States;* orcid.org/0000-0002-0943-7220; Email: dwatkins@olemiss.edu

Authors

Indika Chandrasiri – *Department of Chemistry and Biochemistry, University of Mississippi, University, Mississippi 38677, United States;* orcid.org/0000-0002-4075-4435

Mahesh Loku Yaddehige – *Department of Chemistry and Biochemistry, University of Mississippi, University, Mississippi 38677, United States;* orcid.org/0000-0003-2732-9706

Bo Li – *Department of Chemistry, Southern Methodist University, Dallas, Texas 75205, United States*

Yuzhe Sun – *Department of Mechanical Engineering, Auburn University, Auburn, Alabama 36849, United States;* orcid.org/0000-0002-2572-2339

https://doi.org/10.1021/acsapm.1c01131
ACS Appl. Polym. Mater. XXXX, XXX, XXX–XXX

William E. Meador − *Department of Chemistry and Biochemistry, University of Mississippi, University, Mississippi 38677, United States;* orcid.org/0000-0002-9869-026X
Austin Dorris − *Department of Chemistry and Biochemistry, University of Mississippi, University, Mississippi 38677, United States*
Mohammad Farid Zia − *Department of Biological Sciences, The University of Southern Mississippi, Hattiesburg, Mississippi 39406, United States*
Nathan I. Hammer − *Department of Chemistry and Biochemistry, University of Mississippi, University, Mississippi 38677, United States;* orcid.org/0000-0002-6221-2709
Alex Flynt − *Department of Biological Sciences, The University of Southern Mississippi, Hattiesburg, Mississippi 39406, United States*
Jared H. Delcamp − *Department of Chemistry and Biochemistry, University of Mississippi, University, Mississippi 38677, United States;* orcid.org/0000-0001-5313-4078
Edward Davis − *Department of Mechanical Engineering, Auburn University, Auburn, Alabama 36849, United States;* orcid.org/0000-0001-5413-5398
Alexander Lippert − *Department of Chemistry, Southern Methodist University, Dallas, Texas 75205, United States;* orcid.org/0000-0003-4396-0848

Complete contact information is available at: https://pubs.acs.org/10.1021/acsapm.1c01131

Funding

D.L.W., I.C., A.D., M.F.Z., A.F., N.I.H., W.E.M., and J.H.D. acknowledge NSF award 1757220 for supporting the C5 dye studies.

Notes

The authors declare the following competing financial interest(s): A.L. declares a financial stake in BioLum Sciences, LLC.

■ ACKNOWLEDGMENTS

The authors would like to thank Northwestern University's Atomic and Nanoscale Characterization Experimental Center (NUANCE) and Professor Kwaku Dayie (University of Maryland) for the microscopy images.

■ REFERENCES

(1) Sumer, B.; Gao, J. Theranostic nanomedicine for cancer. *Nanomedicine* **2008**, *3* (2), 137−140.
(2) van der Meel, R.; Vehmeijer, L. J. C.; Kok, R. J.; Storm, G.; van Gaal, E. V. B. Ligand-targeted particulate nanomedicines undergoing clinical evaluation: Current status. *Adv. Drug Delivery Rev.* **2013**, *65* (10), 1284−1298.
(3) Zhang, N.; Xia, Y.; Zou, Y.; Yang, W.; Zhang, J.; Zhong, Z.; Meng, F. ATN-161 Peptide Functionalized Reversibly Cross-Linked Polymersomes Mediate Targeted Doxorubicin Delivery into Melanoma-Bearing C57BL/6 Mice. *Mol. Pharmaceutics* **2017**, *14* (8), 2538−2547.
(4) Moorthy, H.; Govindaraju, T. Dendrimer Architectonics to Treat Cancer and Neurodegenerative Diseases with Implications in Theranostics and Personalized Medicine. *ACS Appl. Bio Mater.* **2021**, *4* (2), 1115−1139.
(5) Talelli, M.; Barz, M.; Rijcken, C. J. F.; Kiessling, F.; Hennink, W. E.; Lammers, T. Core-crosslinked polymeric micelles: Principles, preparation, biomedical applications and clinical translation. *Nano Today* **2015**, *10* (1), 93−117.
(6) Bor, G.; Azmi, I. D. M.; Yaghmur, A. Nanomedicines for cancer therapy: current status, challenges and future prospects. *Ther. Delivery* **2019**, *10* (2), 113−132.
(7) Hinge, N.; Pandey, M. M.; Singhvi, G.; Gupta, G.; Mehta, M.; Satija, S.; Gulati, M.; Dureja, H.; Dua, K. Nanomedicine advances in cancer therapy. In *Advanced 3D-Printed Systems and Nanosystems for Drug Delivery and Tissue Engineering*; Du Toit, L., Kumar, P., Choonara, Y. E., Pillay, V., Eds.; Elsevier, 2020; pp 219−253.
(8) Palivan, C. G.; Goers, R.; Najer, A.; Zhang, X.; Car, A.; Meier, W. Bioinspired polymer vesicles and membranes for biological and medical applications. *Chem. Soc. Rev.* **2016**, *45* (2), 377−411.
(9) Washington, K. E.; Kularatne, R. N.; Karmegam, V.; Biewer, M. C.; Stefan, M. C. Recent advances in aliphatic polyesters for drug delivery applications. *WIREs Nanomed. Nanobi* **2017**, *9* (4), e1446.
(10) Bej, R.; Achazi, K.; Haag, R.; Ghosh, S. Polymersome Formation by Amphiphilic Polyglycerol-b-polydisulfide-b-polyglycerol and Glutathione-Triggered Intracellular Drug Delivery. *Biomacromolecules* **2020**, *21* (8), 3353−3363.
(11) Zhou, Y.; Chen, R.; Yang, H.; Bao, C.; Fan, J.; Wang, C.; Lin, Q.; Zhu, L. Light-responsive polymersomes with a charge-switch for targeted drug delivery. *B J. Mater. Chem.* **2020**, *8* (4), 727−735.
(12) Gitsov, I.; Lambrych, K. R.; Remnant, V. A.; Pracitto, R. Micelles with highly branched nanoporous interior: Solution properties and binding capabilities of amphiphilic copolymers with linear dendritic architecture. *J. Polym. Sci, Part A: Polym. Chem.* **2000**, *38* (15), 2711−2727.
(13) Abad, M.; Martínez-Bueno, A.; Mendoza, G.; Arruebo, M.; Oriol, L.; Sebastián, V.; Piñol, M. Supramolecular Functionalizable Linear−Dendritic Block Copolymers for the Preparation of Nanocarriers by Microfluidics. *Polymers* **2021**, *13* (5), 684.
(14) Adeli, M.; Kakanejadifard, A.; Khani, M.; Bani, F.; Kabiri, R.; Sadeghizad, M. A polyglycerol−polycaprolactone−polycitric acid copolymer and its self-assembly to produce medium-responsive nanoparticles. *B J. Mater. Chem.* **2014**, *2* (23), 3589−3596.
(15) Danson, S.; Ferry, D.; Alakhov, V.; Margison, J.; Kerr, D.; Jowle, D.; Brampton, M.; Halbert, G.; Ranson, M. Phase I dose escalation and pharmacokinetic study of pluronic polymer-bound doxorubicin (SP1049C) in patients with advanced cancer. *Br. J. Cancer* **2004**, *90* (11), 2085−2091.
(16) Rijcken, C. J.; Snel, C. J.; Schiffelers, R. M.; van Nostrum, C. F.; Hennink, W. E. Hydrolysable core-crosslinked thermosensitive polymeric micelles: Synthesis, characterisation and in vivo studies. *Biomaterials* **2007**, *28* (36), 5581−5593.
(17) Yorulmaz Avsar, S.; Kyropoulou, M.; Di Leone, S.; Schoenenberger, C.-A.; Meier, W. P.; Palivan, C. G. Biomolecules Turn Self-Assembling Amphiphilic Block Co-polymer Platforms Into Biomimetic Interfaces. *Front. Chem.* **2019**, *6* (645), 1.
(18) Rideau, E.; Dimova, R.; Schwille, P.; Wurm, F. R.; Landfester, K. Liposomes and polymersomes: a comparative review towards cell mimicking. *Chem. Soc. Rev.* **2018**, *47* (23), 8572−8610.
(19) Cabral, H.; Miyata, K.; Osada, K.; Kataoka, K. Block Copolymer Micelles in Nanomedicine Applications. *Chem. Rev.* **2018**, *118* (14), 6844−6892.
(20) Yorulmaz Avsar, S.; Kyropoulou, M.; Di Leone, S.; Schoenenberger, C. A.; Meier, W. P.; Palivan, C. G. Biomolecules Turn Self-Assembling Amphiphilic Block Co-polymer Platforms Into Biomimetic Interfaces. *Front Chem.* **2019**, *6*, 645.
(21) Deng, C.; Jiang, Y.; Cheng, R.; Meng, F.; Zhong, Z. Biodegradable polymeric micelles for targeted and controlled anticancer drug delivery: Promises, progress and prospects. *Nano Today* **2012**, *7* (5), 467−480.
(22) Zheng, Y.; Thurecht, K. J.; Chen, X.; Roberts, C. J.; Irvine, D. J.; Howdle, S. M.; Wang, W. In situ formation of crosslinked core−corona polymeric nanoparticles from a novel hyperbranched core. *Polym. Chem.* **2012**, *3* (10), 2807−2814.
(23) Palanikumar, L.; Al-Hosani, S.; Kalmouni, M.; Nguyen, V. P.; Ali, L.; Pasricha, R.; Barrera, F. N.; Magzoub, M. pH-responsive high stability polymeric nanoparticles for targeted delivery of anticancer therapeutics. *Commun. Biol.* **2020**, *3* (1), 95.

(24) Zuo, H.; Gu, Z.; Cooper, H.; Xu, Z. P. Crosslinking to enhance colloidal stability and redispersity of layered double hydroxide nanoparticles. *J. Colloid Interface Sci.* **2015**, *459*, 10−16.
(25) Buwalda, S.; Al Samad, A.; El Jundi, A.; Bethry, A.; Bakkour, Y.; Coudane, J.; Nottelet, B. Stabilization of poly(ethylene glycol)-poly(ε-caprolactone) star block copolymer micelles via aromatic groups for improved drug delivery properties. *J. Colloid Interface Sci.* **2018**, *514*, 468−478.
(26) Hu, Q.; Rijcken, C. J. F.; van Gaal, E.; Brundel, P.; Kostkova, H.; Etrych, T.; Weber, B.; Barz, M.; Kiessling, F.; Prakash, J.; Storm, G.; Hennink, W. E.; Lammers, T. Tailoring the physicochemical properties of core-crosslinked polymeric micelles for pharmaceutical applications. *J. Controlled Release* **2016**, *244*, 314−325.
(27) Lin, M.; Dai, Y.; Xia, F.; Zhang, X. Advances in non-covalent crosslinked polymer micelles for biomedical applications. *Mater. Sci. Eng. C* **2021**, *119*, 111626.
(28) Mavila, S.; Eivgi, O.; Berkovich, I.; Lemcoff, N. G. Intramolecular Cross-Linking Methodologies for the Synthesis of Polymer Nanoparticles. *Chem. Rev.* **2016**, *116* (3), 878−961.
(29) Chandrasiri, I.; Abebe, D. G.; Loku Yaddehige, M.; Williams, J. S. D.; Zia, M. F.; Dorris, A.; Barker, A.; Simms, B. L.; Parker, A.; Vinjamuri, B. P.; Le, N.; Gayton, J. N.; Chougule, M. B.; Hammer, N. I.; Flynt, A.; Delcamp, J. H.; Watkins, D. L. Self-Assembling PCL−PAMAM Linear Dendritic Block Copolymers (LDBCs) for Bioimaging and Phototherapeutic Applications. *ACS Appl. Bio Mater.* **2020**, *3* (9), 5664−5677.
(30) Gitsov, I. Hybrid linear dendritic macromolecules: From synthesis to applications. *J. Polym. Sci, Part A: Polym. Chem.* **2008**, *46* (16), 5295−5314.
(31) Blasco, E.; Piñol, M.; Oriol, L. Responsive linear-dendritic block copolymers. *Macromol. Rapid Commun.* **2014**, *35* (12), 1090−115.
(32) Chandrasiri, I.; Abebe, D. G.; Gupta, S.; Williams, J. S. D.; Rieger, W. D.; Simms, B. L.; Yaddehige, M. L.; Noh, Y.; Payne, M. E.; Fortenberry, A. W.; Smith, A. E.; Ilavsky, J.; Grayson, S. M.; Schneider, G. J.; Watkins, D. L. Synthesis and characterization of polylactide-PAMAM "Janus-type" linear-dendritic hybrids. *J. Polym. Sci, Part A: Polym. Chem.* **2019**, *57* (13), 1448−1459.
(33) Yaddehige, M. L.; Chandrasiri, I.; Barker, A.; Kotha, A. K.; Dal Williams, J. S.; Simms, B.; Kucheryavy, P.; Abebe, D. G.; Chougule, M. B.; Watkins, D. L. Structural and Surface Properties of Polyamidoamine (PAMAM) − Fatty Acid-based Nanoaggregates Derived from Self-assembling Janus Dendrimers. *ChemNanoMat* **2020**, *6* (12), 1833−1842.
(34) Percec, V.; Wilson, D. A.; Leowanawat, P.; Wilson, C. J.; Hughes, A. D.; Kaucher, M. S.; Hammer, D. A.; Levine, D. H.; Kim, A. J.; Bates, F. S.; Davis, K. P.; Lodge, T. P.; Klein, M. L.; DeVane, R. H.; Aqad, E.; Rosen, B. M.; Argintaru, A. O.; Sienkowska, M. J.; Rissanen, K.; Nummelin, S.; Ropponen, J. Self-Assembly of Janus Dendrimers into Uniform Dendrimersomes and Other Complex Architectures. *Science* **2010**, *328* (5981), 1009−1014.
(35) del Barrio, J.; Oriol, L.; Sánchez, C.; Serrano, J. L.; Di Cicco, A.; Keller, P.; Li, M.-H. Self-Assembly of Linear−Dendritic Diblock Copolymers: From Nanofibers to Polymersomes. *J. Am. Chem. Soc.* **2010**, *132* (11), 3762−3769.
(36) Liu, X.; Gitsov, I. Nonionic Amphiphilic Linear Dendritic Block Copolymers. Solvent-Induced Self-Assembly and Morphology Tuning. *Macromolecules* **2019**, *52* (15), 5563−5573.
(37) Mai, Y.; Eisenberg, A. Self-assembly of block copolymers. *Chem. Soc. Rev.* **2012**, *41* (18), 5969−5985.
(38) Remant Bahadur, K. C.; Bhattarai, S. R.; Aryal, S.; Khil, M. S.; Dharmaraj, N.; Kim, H. Y. Novel amphiphilic triblock copolymer based on PPDO, PCL, and PEG: Synthesis, characterization, and aqueous dispersion. *Colloids Surf. A: Physicochem. Eng. Asp.* **2007**, *292* (1), 69−78.
(39) Gayton, J.; Autry, S. A.; Meador, W.; Parkin, S. R.; Hill, G. A.; Hammer, N. I.; Delcamp, J. H. Indolizine-Cyanine Dyes: Near Infrared Emissive Cyanine Dyes with Increased Stokes Shifts. *J. Org. Chem.* **2019**, *84* (2), 687−697.
(40) Peris, G.; Miller, S. J. A Nonenzymatic Acid/Peracid Catalytic Cycle for the Baeyer−Villiger Oxidation. *Org. Lett.* **2008**, *10* (14), 3049−3052.
(41) Goddard, E. D.; Turro, N. J.; Kuo, P. L.; Ananthapadmanabhan, K. P. Fluorescence probes for critical micelle concentration determination. *Langmuir* **1985**, *1* (3), 352−355.
(42) Kalyanasundaram, K.; Thomas, J. K. Environmental effects on vibronic band intensities in pyrene monomer fluorescence and their application in studies of micellar systems. *J. Am. Chem. Soc.* **1977**, *99* (7), 2039−2044.
(43) Chen, J.; Dai, W. T.; He, Z. M.; Gao, L.; Huang, X.; Gong, J. M.; Xing, H. Y.; Chen, W. D. Fabrication and Evaluation of Curcumin-loaded Nanoparticles Based on Solid Lipid as a New Type of Colloidal Drug Delivery System. *Indian J. Pharm. Sci.* **2013**, *75* (2), 178−184.
(44) Maiuri, M.; Garavelli, M.; Cerullo, G. Ultrafast Spectroscopy: State of the Art and Open Challenges. *J. Am. Chem. Soc.* **2020**, *142* (1), 3−15.
(45) Sun, Y.; Davis, E. W. Facile fabrication of polydopamine nanotubes for combined chemo-photothermal therapy. *B J. Mater. Chem.* **2019**, *7* (43), 6828−6839.
(46) Ballesteros, C. A. S.; Correa, D. S.; Zucolotto, V. Polycaprolactone nanofiber mats decorated with photoresponsive nanogels and silver nanoparticles: Slow release for antibacterial control. *Mater. Sci. Eng. C* **2020**, *107*, 110334.
(47) Girgis, N. S. G. Formulation and Evaluation of Atorvastatin Calcium-Poly-ε-Caprolactone Nanoparticles Loaded Ocular Inserts for Sustained Release and Antiinflammatory Efficacy. *Curr. Pharm. Biotechnol.* **2020**, *21* (15), 1688−1698.
(48) Perveen, R.; Inamuddin; Nasar, A. Multiwalled carbon nanotube-based nanocomposites for artificial bone grafting. In *Applications of Nanocomposite Materials in Orthopedics*, Inamuddin, Asiri, A. M., Mohammad, A., Eds.; Woodhead Publishing, 2019; pp 111−126.
(49) Izraylit, V.; Hommes-Schattmann, P. J.; Neffe, A. T.; Gould, O. E. C.; Lendlein, A. Alkynyl-functionalized chain-extended PCL for coupling to biological molecules. *Eur. Polym. J.* **2020**, *136*, 109908.
(50) Hua, C.; Dong, C.-M.; Wei, Y. Versatile Strategy for the Synthesis of Dendronlike Polypeptide/Linear Poly(ε-caprolactone) Block Copolymers via Click Chemistry. *Biomacromolecules* **2009**, *10* (5), 1140−1148.
(51) Dong, C.-M.; Liu, G. Linear−dendritic biodegradable block copolymers: from synthesis to application in bionanotechnology. *Polym. Chem.* **2013**, *4* (1), 46−52.
(52) Gadomska-Gajadhur, A.; Ruśkowski, P. Biocompatible Catalysts for Lactide Polymerization—Catalyst Activity, Racemization Effect, and Optimization of the Polymerization Based On Design of Experiments. *Org. Process Res. Dev.* **2020**, *24* (8), 1435−1442.
(53) Johnson, P. M.; Kundu, S.; Beers, K. L. Modeling Enzymatic Kinetic Pathways for Ring-Opening Lactone Polymerization. *Biomacromolecules* **2011**, *12* (9), 3337−3343.
(54) Liu, X.; Monzavi, T.; Gitsov, I. Controlled ATRP Synthesis of Novel Linear-Dendritic Block Copolymers and Their Directed Self-Assembly in Breath Figure Arrays. *Polymers* **2019**, *11* (3), 539.
(55) Cerrai, P.; Tricoli, M.; Andruzzi, F.; Paci, M.; Paci, M. Polyether-polyester block copolymers by non-catalysed polymerization of ε-caprolactone with poly(ethylene glycol). *Polymer* **1989**, *30* (2), 338−343.
(56) Trovati, G.; Sanches, E. A.; Neto, S. C.; Mascarenhas, Y. P.; Chierice, G. O. Characterization of polyurethane resins by FTIR, TGA, and XRD. *J. Appl. Polym. Sci.* **2010**, *115* (1), 263−268.
(57) Vleugels, M. E. J.; de Zwart, M. E.; Magana, J. R.; Lamers, B. A. G.; Voets, I. K.; Meijer, E. W.; Petkau-Milroy, K.; Palmans, A. R. A. Effects of crystallinity and dispersity on the self-assembly behavior of block co-oligomers in water. *Polym. Chem.* **2020**, *11* (45), 7170−7177.
(58) Kim, S.; Shi, Y.; Kim, J. Y.; Park, K.; Cheng, J.-X. Overcoming the barriers in micellar drug delivery: loading efficiency, in vivo

https://doi.org/10.1021/acsapm.1c01131
ACS Appl. Polym. Mater. XXXX, XXX, XXX−XXX

stability, and micelle−cell interaction. *Expert Opin. Drug Deliv* **2010**, *7* (1), 49−62.
(59) Fröhlich, E. The role of surface charge in cellular uptake and cytotoxicity of medical nanoparticles. *Int. J. Nanomedicine* **2012**, *7*, 5577.
(60) Blanco, E.; Shen, H.; Ferrari, M. Principles of nanoparticle design for overcoming biological barriers to drug delivery. *Nat. Biotechnol.* **2015**, *33* (9), 941−51.
(61) Liu, R. *Water-insoluble drug formulation*; CRC press, 2000.
(62) Batrakova, E.; Lee, S.; Li, S.; Venne, A.; Alakhov, V.; Kabanov, A. Fundamental Relationships Between the Composition of Pluronic Block Copolymers and Their Hypersensitization Effect in MDR Cancer Cells. *Pharm. Res.* **1999**, *16* (9), 1373−1379.
(63) Lu, Y.; Zhang, E.; Yang, J.; Cao, Z. Strategies to improve micelle stability for drug delivery. *Nano Research* **2018**, *11* (10), 4985−4998.
(64) Israelachvili, J. N.; Mitchell, D. J.; Ninham, B. W. Theory of self-assembly of lipid bilayers and vesicles. *Biochim Biophys Acta Biomembr* **1977**, *470* (2), 185−201.
(65) Zhao, J.; Nagao, S.; Odegard, G. M.; Zhang, Z.; Kristiansen, H.; He, J. Size-dependent mechanical behavior of nanoscale polymer particles through coarse-grained molecular dynamics simulation. *Nanoscale Res. Lett.* **2013**, *8* (1), 541.
(66) Yao, Y.; Wei, Y.; Chen, S. Size effect of the surface energy density of nanoparticles. *Surf. Sci.* **2015**, *636*, 19−24.
(67) Singer, A.; Barakat, Z.; Mohapatra, S.; Mohapatra, S. S. Nanoscale Drug-Delivery Systems: In Vitro and In Vivo Characterization. In *Nanocarriers for Drug Delivery*; Mohapatra, S. S., Ranjan, S., Dasgupta, N., Mishra, R. K., Thomas, S., Eds.; Elsevier, 2019; Chapter 13, pp 395−419.
(68) Karthikeyan, A.; Senthil, N.; Min, T. Nanocurcumin: A Promising Candidate for Therapeutic Applications. *Front. Pharmacol.* **2020**, *11* (487), 1.
(69) Lu, H.; Du, S. A phenomenological thermodynamic model for the chemo-responsive shape memory effect in polymers based on Flory−Huggins solution theory. *Polym. Chem.* **2014**, *5* (4), 1155−1162.
(70) Liu, J.; Xiao, Y.; Allen, C. Polymer-drug compatibility: A guide to the development of delivery systems for the anticancer agent, ellipticine. *J. Pharm. Sci.* **2004**, *93* (1), 132−143.
(71) Delcamp, J. H.; Shi, Y.; Yum, J.-H.; Sajoto, T.; Dell'Orto, E.; Barlow, S.; Nazeeruddin, M. K.; Marder, S. R.; Grätzel, M. The Role of π Bridges in High-Efficiency DSCs Based on Unsymmetrical Squaraines. *Chem.—Eur. J.* **2013**, *19* (5), 1819−1827.
(72) Fonte, P.; Reis, S.; Sarmento, B. Facts and evidences on the lyophilization of polymeric nanoparticles for drug delivery. *J. Controlled Release* **2016**, *225*, 75−86.
(73) Kim, H. S.; Wainer, I. W. Simultaneous analysis of liposomal doxorubicin and doxorubicin using capillary electrophoresis and laser induced fluorescence. *J. Pharm. Biomed Anal* **2010**, *52* (3), 372−376.
(74) Suk, J. S.; Xu, Q.; Kim, N.; Hanes, J.; Ensign, L. M. PEGylation as a strategy for improving nanoparticle-based drug and gene delivery. *Adv. Drug Delivery Rev.* **2016**, *99*, 28−51.
(75) Hu, Y.; Gong, X.; Zhang, J.; Chen, F.; Fu, C.; Li, P.; Zou, L.; Zhao, G. Activated charge-reversal polymeric nano-system: the promising strategy in drug delivery for cancer therapy. *Polymers* **2016**, *8* (4), 99.
(76) Pelaz, B.; del Pino, P.; Maffre, P.; Hartmann, R.; Gallego, M.; Rivera-Fernández, S.; de la Fuente, J. M.; Nienhaus, G. U.; Parak, W. J. Surface Functionalization of Nanoparticles with Polyethylene Glycol: Effects on Protein Adsorption and Cellular Uptake. *ACS Nano* **2015**, *9* (7), 6996−7008.
(77) Lynch, I.; Dawson, K. A. Protein-nanoparticle interactions. *Nano Today* **2008**, *3* (1), 40−47.
(78) Ingle, N. P.; Hexum, J. K.; Reineke, T. M. Polyplexes Are Endocytosed by and Trafficked within Filopodia. *Biomacromolecules* **2020**, *21* (4), 1379−1392.
(79) Simms, B. L.; Ji, N.; Chandrasiri, I.; Zia, M. F.; Udemgba, C. S.; Kaur, R.; Delcamp, J. H.; Flynt, A.; Tan, C.; Watkins, D. L. Physicochemical properties and bio-interfacial interactions of surface modified PDLLA-PAMAM linear dendritic block copolymers. *J. Polym. Sci.* **2021**, *59* (19), 2177−2192.

https://doi.org/10.1021/acsapm.1c01131
ACS Appl. Polym. Mater. XXXX, XXX, XXX−XXX